

CHALMERS



Final Report on the Research Project Ringhals Diagnostics and Monitoring Stage 14

I. PÁZSIT
C. MONTALVO MARTÍN
V. DYKIN
H. NYLÉN

Department of Nuclear Engineering
CHALMERS UNIVERSITY OF TECHNOLOGY
Göteborg, Sweden 2011

CTH-NT-253/RR-16

December 2011

**Final Report on the Research Project
Ringhals Diagnostics and Monitoring
Stage 14**

I. Pázsit, C. Montalvo Martín, V. Dykin and H. Nylén

**Department of Nuclear Engineering
Chalmers University of Technology
SE-412 96 Göteborg, Sweden
ISSN 0281-9775**

Final Report on the Research Project Ringhals Diagnostics and Monitoring Stage 14

I. Pázsit, C. Montalvo Martín, V. Dykin and H. Nylén

**Department of Nuclear Engineering, Chalmers University of Technology
SE-412 96 Göteborg, Sweden**

Abstract

This report gives an account of the work performed by the Department of Nuclear Engineering, Chalmers, in the frame of a research contract with Ringhals, Vattenfall AB, contract No. 614061-002. The contract constitutes Stage 14 of a long-term co-operative research work concerning diagnostics and monitoring of the BWR and PWR units. The work in Stage 14 has been performed between January 1st, and December 31st, 2011. In Stage 14 we have worked with three items as follows:

1. Analysis of three new ex-core measurements, taken at BOC, MOC and EOC, with the new curve fitting procedure;
2. An investigation of the ultra-low frequency oscillations in reactor power in R3 and R4;
3. Further development of the theory and simulations in order to determine the void content in R1 from the analysis of in-core measurements.

This work was performed at the Department of Nuclear Engineering, Chalmers University of Technology by Imre Pázsit (project leader), Cristina Montalvo Martín (visitor from the Technical University of Madrid), Victor Dykin and Henrik Nylén, who was also the contact person at Ringhals.

Contents

1. INTRODUCTION	1
2. ANALYSIS OF THREE NEW EX-CORE MEASUREMENTS, TAKEN AT BOC, MOC AND EOC, WITH THE NEW CURVE FITTING PROCEDURE	1
2.1. The curve fitting procedure	5
2.2. Results of the measurements in Stage 14	5
2.3. Conclusions, further work	9
3. AN INVESTIGATION OF THE ULTRA-LOW FREQUENCY OSCILLATIONS IN REACTOR POWER IN R3 AND R4	9
4. FURTHER DEVELOPMENT OF THE THEORY AND SIMULATIONS TO DETERMINE VOID CONTENT IN R3 FROM THE ANALYSIS OF IN-CORE NEUTRON NOISE MEASUREMENTS	14
4.1. Introduction	14
4.2. Model construction	15
4.3. Principles of the simulation	16
4.4. Determination of the void content: methods	18
4.4.1. APSD break-frequency approach	18
4.4.2. Transit time approach	21
4.5. Simulation results	24
4.6. Conclusions	32
5. PROPOSAL FOR STAGE 15	32
6. ACKNOWLEDGEMENT	32
7. REFERENCES	32

1. INTRODUCTION

The long term goal of the contract is to utilize the research potential of the Department of Nuclear Engineering at Chalmers in treating reactor physics problems related to the operation of the power plant. This is achieved in a co-operative research project, in the course of which the understanding of relevant problems increases at the department as well as methods are elaborated and implemented for their solution. The results obtained in the earlier stages have been reported in [1]-[14].

The work in Stage 14 has been performed between January 1st, and December 31st, 2011. In Stage 14 we have worked with three items as follows:

1. Analysis of three new ex-core measurements, taken at BOC, MOC and EOC, with the new curve fitting procedure;
2. An investigation of the ultra-low frequency oscillations in reactor power in R3 and R4
3. Further development of the theory and simulations in order to determine the void content in R1 from the analysis of in-core measurements.

A further general objective of the work is to gain experience with the important and characteristic features of power spectra and certain operational variables in the normal state, in order to be able to perform diagnostics of various phenomena.

A proposal for the continuation of the work in Stage 15 is also given at the end of this report.

2. ANALYSIS OF THREE NEW EX-CORE MEASUREMENTS, TAKEN AT BOC, MOC AND EOC, WITH THE NEW CURVE FITTING PROCEDURE

In Stage 12 a hypothesis was formulated for the explanation of the increase of the amplitude of the 8 Hz peak in the ex-core neutron detector spectra within the cycle, which re-starts after each refueling. The hypothesis is based on the assumption that the vibration peak is actually a double peak, corresponding to two vibration modes with different physical origins. An illustration of the double peak is shown in Fig. 1, which shows the Auto Power Spectral Density of an ex-core detector, taken in Ringhals-4. The hypothesis is then that around the frequency range of the beam mode, there are two modes of vibration: Mode 1, around 7 Hz, which is related to the core barrel motion itself, and Mode 2, around 8 Hz, corresponding to flow induced vibrations of single fuel assemblies. Out of the two modes, only the amplitude of Mode 2 is increasing during the cycle. The increase can be induced either with the amplitude increase of the fuel assembly vibrations (which might be understood as being due to changed mechanical properties of the fuel pins due to burn-up), or to the change of the conversion factor between mechanical vibrations of fuel assemblies and the induced neutron noise, as measured by ex-core detectors. This latter possibility was

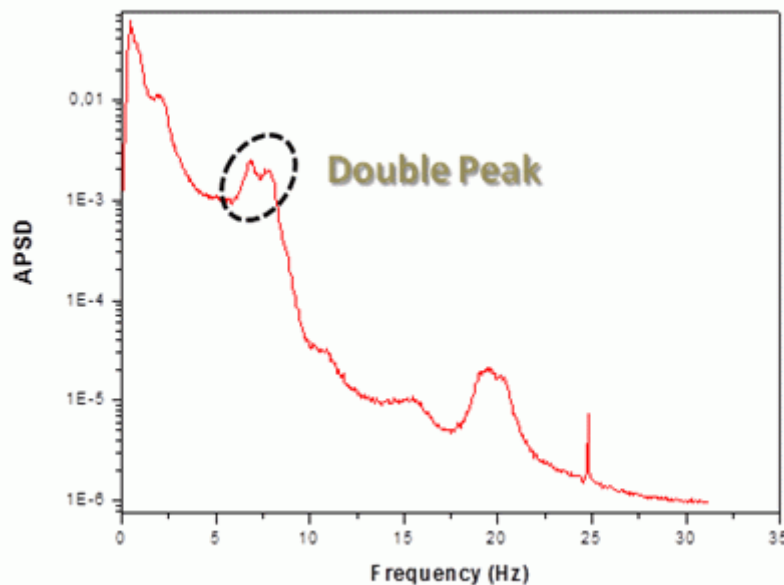


Fig. 1 APSD on an ex-core neutron detector, taken in Ringhals-4

suggested by Sweeney et al [16] and its feasibility is under investigation through core physics calculations in Chalmers.

Since the analysis made in Stage 12 was the first of its kind, it was planned to confirm it in a second measurement campaign, in Stage 13. To this order three ex-core measurements were made during the next fuel cycle in Ringhals-4. The results of the analysis were reported in Ref. [14]. However, from these measurements, it was not possible to confirm the hypothesis of Stage 12 about the long-term trend behaviour of the two peaks around 7 and 8 Hz. This is because there was a total time span of only 3 months between these three measurements, made towards the end of the cycle. Three months is a too short time interval to estimate the behaviour of the two different modes of vibration of the beam bode, especially in view of the fact that according to the findings of Stage 12, the increase of the amplitude of the APSDs is the fastest at the beginning of the cycle, and it slows down towards the end of the cycle.

It was therefore planned that in the present Stage, three more measurements will be made and analysed, with a sufficient time span between those three. According to the plans, three measurements would be performed, one each at BOC, MOC and EOC. The first two were indeed performed in January and June 2011, respectively, in Ringhals-3. The third measurement was planned at the end of cycle in late August or September. However, the third measurement was not performed because of a temporary shutdown of the reactor during September and October. Hence, once again, the planned confirmation of the hypothesis with the analysis of three measurements covering the whole fuel cycle was not possible.

One further circumstance regarding the measurements analysed in the present report is that unlike those in the previous two Stages, these were made in Ringhals-3. It turns out that the peak structure at the beam mode frequency around 8 Hz is different between R3 and R4. Whereas in R4 there is a clear visible separation of two peaks (c.f. Fig. 1), in R3 the two peaks are much less distinguishable, which has a consequence on the accuracy of the analysis results, as it will be shown later.

The sampling frequency in the present measurements was 62.5 Hz, the same as the one used in previous stages for this analysis. Some basic data of the two measurements analyzed are summarized below in Table 1. The measurements were made with the same settings and general parameters as those in the previous Stage [17].

Table 1 Some data of the measurements in Ringhals 3

Channel	Measurement 21st January 2011	Measurement 16th June 2011
0	Time	Time
1	N41U DC	N41U DC
2	N42U DC	N42U DC
3	N43U DC	N43U DC
4	N44U DC	N44U DC
5	N41L DC	N41L DC
6	N42L DC	N42L DC
7	N43L DC	N43L DC
8	N44L DC	N44L DC
9	N41U AC	N41U AC
10	N42U AC	N42U AC
11	N43U AC	N43U AC
12	N44U AC	N44U AC
13	N41L AC	N41L AC
14	N42L AC	N42L AC
15	N43L AC	N43L AC
16	N44L AC	N44L AC

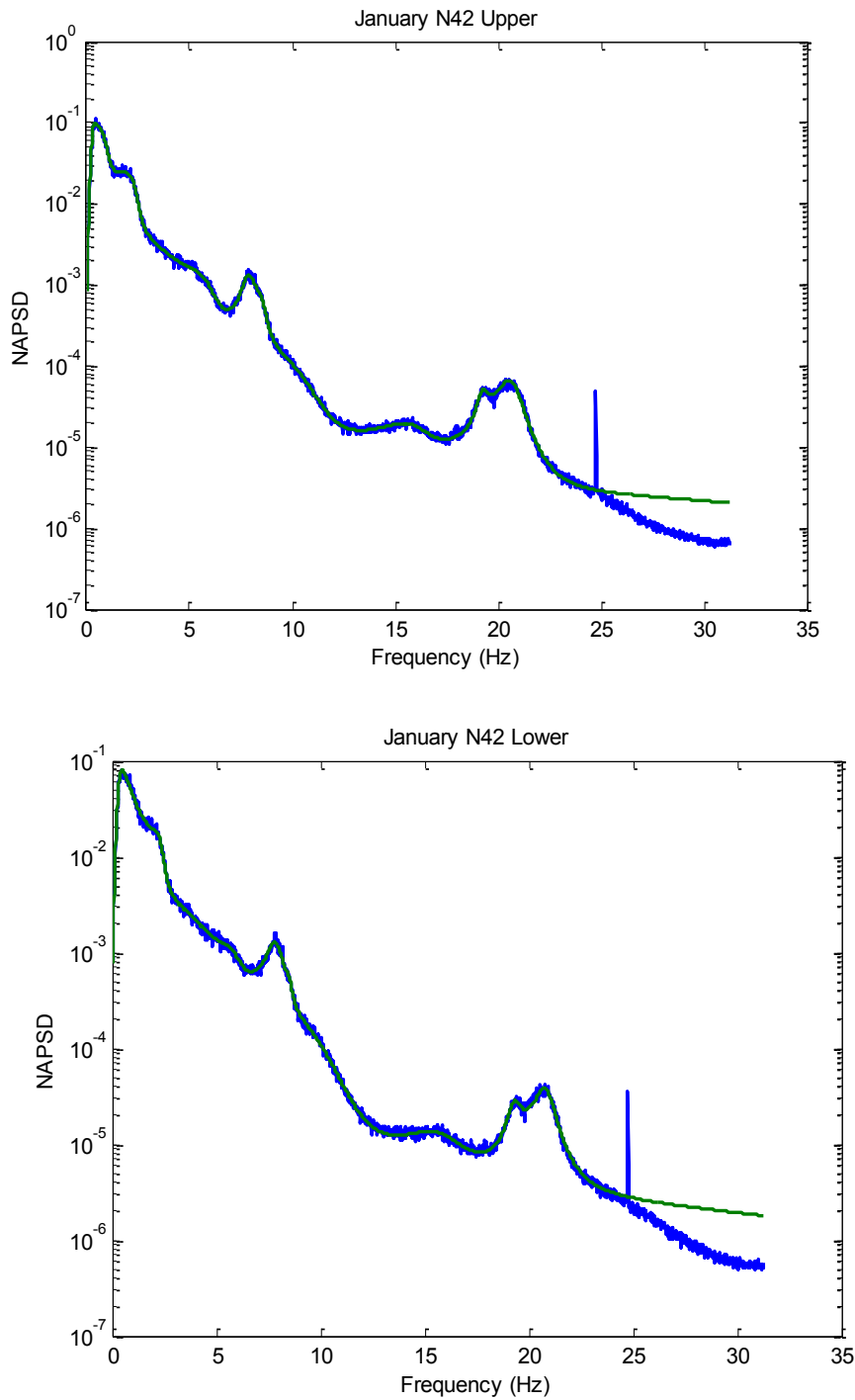


Fig. 2 APSDs of the detectors N42 Upper (upper figure) and N42 Lower (lower figure) from the measurement taken in January 2011 at Ringhals 3

2.1. The curve fitting procedure

The fitting procedure is based on a Breit-Wigner formula taken from [15]:

$$APSD(\omega) = \sum_{\lambda} \left\{ \frac{\mu_{\lambda} A_{\lambda} + (\omega - \nu_{\lambda}) B_{\lambda}}{\mu_{\lambda}^2 + (\omega - \nu_{\lambda})^2} + \frac{\mu_{\lambda} A_{\lambda} - (\omega - \nu_{\lambda}) B_{\lambda}}{\mu_{\lambda}^2 + (\omega + \nu_{\lambda})^2} \right\} \quad (1)$$

Each resonance is characterized by a group of four parameters: the pole strength A_{λ} , frequency ν , damping μ_{λ} and skewness B_{λ} . This last parameter determines the overlapping between resonances which increases along the cycle. It is this parameter which makes the formula a very effective tool, because it makes possible to resolve strongly overlapping resonances, the identification of which is otherwise very difficult.

Another advantage of this fitting procedure is that in the conventional fitting procedures, such as those based on a model of a damped linear oscillator, one needs to assume a certain form for the background, which introduces some arbitrariness into the procedure. The present fitting procedure eliminates this arbitrariness because the background is composed of the “tails” of all of the resonances. On the other hand, a characteristic of this fitting procedure is that it needs to be performed by an expert who has a certain idea of the initial values for the parameters. Besides, in order to succeed in the fitting process, it is necessary to assume more peaks than what is visible at first sight.

Once the fitting is achieved, a trend analysis is performed for the peaks of the frequencies of interest. Since we are interested in the beam mode, its amplitude can be monitored and surveyed along the cycle. The hypothesis based on the fact that two different peaks can be distinguished in the range of the beam mode: Mode 1, around 7 Hz and Mode 2 around 8 Hz (Fig. 1). The results arising from the fitted values are used to characterize these two modes in order to understand the increasing amplitude behaviour of the beam mode.

In Fig. 2 two examples of the fitted spectra of two detectors N42U and N42L are shown. The results of the curve fitting, in form of the values of the fitted parameters, are shown in Table 2. Only the values for the frequencies around 8 Hz, marked with yellow in the Table, will be used for the analysis.

2.2. Results of the measurements in Stage 14

The measurements of this Stage correspond to cycle 28 of Ringhals 3, i.e. in a different core than in the previous two Stages. The first measurement is from January 2011 and the second and last measurement from June 2011. Both of them belong to the same cycle and are separated sufficiently in time in order to appreciate the evolution of the amplitudes of the different modes. In the previous Stage, the amplitudes were evaluated for all the lowers detectors in a certain combination as indicated in Eqs (2) and (3):

Table 2 Fitted parameters for the detectors N42U and N42L

N42 U		January			
Number of peaks	Frequency	Damping	Amplitude	Skewness	
1	2.65E-01	1.78E-01	5.07E-03	1.40E-02	
2	8.87E-01	3.85E-01	6.58E-03	-1.63E-02	
3	2.36E+00	4.34E-01	6.70E-07	-5.38E-03	
4	1.70E+00	1.29E+00	2.37E-02	-1.59E-03	
5	5.89E+00	9.34E-01	1.36E-04	-6.71E-04	
6	7.88E+00	3.73E-01	3.62E-04	-2.80E-05	
7	8.52E+00	3.34E-01	9.15E-05	-7.48E-05	
8	1.01E+01	1.96E+00	3.32E-05	-1.83E-04	
9	1.60E+01	1.42E+00	1.01E-05	-1.11E-05	
10	1.92E+01	3.39E-01	9.44E-06	2.46E-06	
11	2.07E+01	6.57E-01	3.75E-05	-1.20E-05	

N42 L		January			
Number of peaks	Frequency	Damping	Amplitude	Skewness	
1	2.72E-01	2.48E-01	2.37E-05	2.04E-02	
2	8.23E-02	1.12E+00	2.72E-02	-2.30E-01	
3	2.32E+00	3.38E-01	1.52E-03	-2.91E-03	
4	3.68E+00	2.15E+00	1.03E-03	-2.26E-03	
5	5.84E+00	5.99E-01	1.35E-04	-1.77E-04	
6	7.87E+00	4.57E-01	4.51E-04	-1.27E-04	
7	8.54E+00	1.54E-01	1.67E-05	-1.20E-05	
8	9.93E+00	1.91E+00	3.63E-05	-1.82E-04	
9	1.59E+01	1.70E+00	9.59E-06	-8.04E-06	
10	1.93E+01	4.03E-01	7.31E-06	1.27E-06	
11	2.08E+01	5.62E-01	1.82E-05	-3.74E-06	

$$\mu x(t) = \frac{1}{2}(\delta\phi_{41}(t) - \delta\phi_{42}(t)), \quad (2)$$

$$\mu y(t) = \frac{1}{2}(\delta\phi_{43}(t) - \delta\phi_{44}(t)) \quad (3)$$

Here, $\delta\phi_{41}$, $\delta\phi_{42}$, $\delta\phi_{43}$ and $\delta\phi_{44}$ stand for the neutron noise from detectors N41, N42, N43 and N44 respectively, μ is the scaling factor between the neutron noise and the mechanical vibrations, and $x(t)$ and $y(t)$ are the components of the beam mode vibrations.

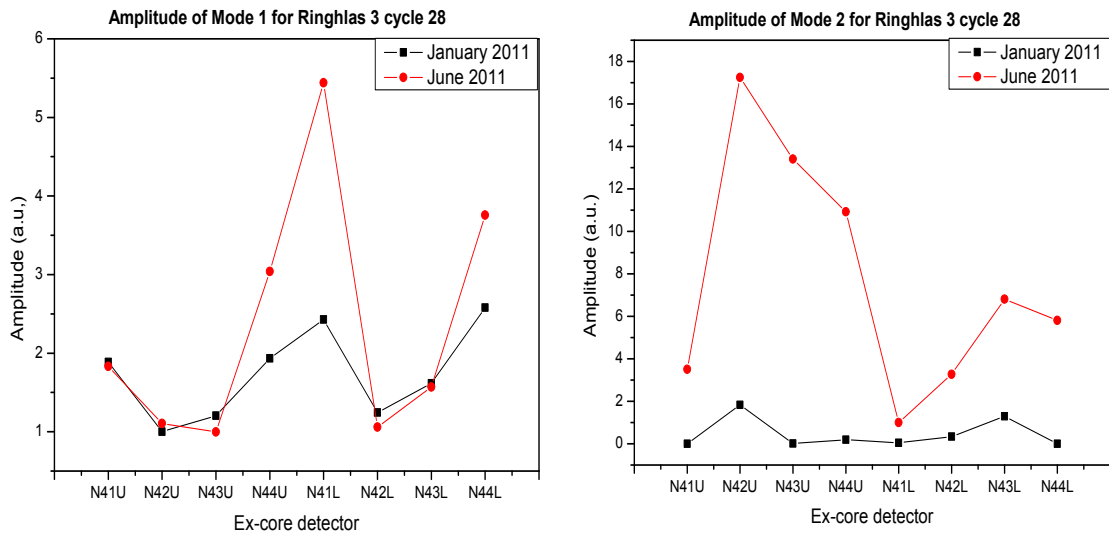


Fig. 3 Trend analysis of the amplitudes of Mode 1 and Mode 2 in Stage 14 for all ex-core detectors

The combinations in Eqs (2) and (3) were originally introduced to enhance the weight of the beam mode vibrations of the core barrel in the ex-core detectors, and has been used for the analysis of the core barrel vibration analysis during a long time in the past. However, it was recognised in the previous Stage [14] that is more correct to evaluate the amplitudes individually for each detector. The reason for this is that one of the modes is supposed to be linked to the fuel assembly vibrations. The combination of the detector signals, expressed in Eqs (2) and (3), is based on symmetry considerations of the ex-core noise as induced purely by the core barrel vibrations. The ex-core noise induced by individual vibrations of the fuel assemblies, on the other hand, does not show such symmetries at all (except for the singular case of a fuel assembly vibrating in the geometrical centre of a core with complete azimuthal symmetry). Neither the phase nor the amplitude relationships between opposite detectors will show the same symmetry properties as that of the pendular motion of the core barrel, rather these will be much more complicated and moreover will depend on the position of the vibrating fuel element in the core and the vibration pattern in space.

The results of the trend analysis from this Stage are shown in Fig. 3. According to the above, the analysis was performed for each detector separately. The left hand side figure shows the development of the amplitude of Mode 1, and the r.h.s. figure that of Mode 2. The trend analysis (temporal evolution of the amplitudes) is made by comparing the values of the black curve (representing the data in the January measurements) with those of the red curve (data from the June measurements). The difference represents the evolution of the amplitude, shown for all 8 detectors (4 upper and 4 lower), respectively.

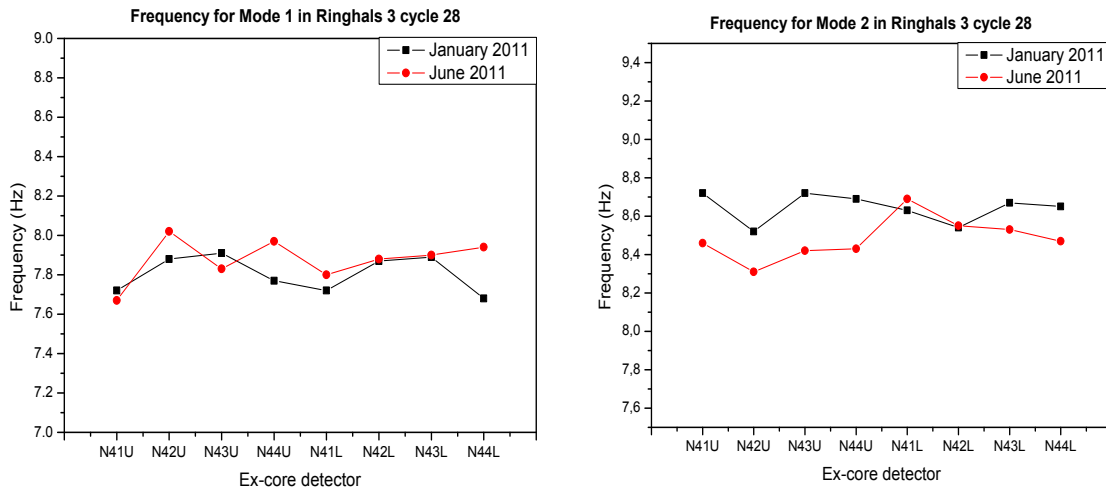


Fig. 4 Trend analysis of the frequencies of Mode 1 and Mode 2 in Stage 14 for all ex-core detectors

The results of this analysis, which are only based on two measurements, are not as decisive as in the previous measurements, but are in a relatively good agreement with those. For Mode 1, the change of the amplitude is zero or negative, except for one of the detectors which shows a large deviation and two others showing a moderate increase. The change of Mode 2 is more significant. There is an increase in all signals, out of which five can be classified as considerable. These results are not as convincing as those from the previous Stages, but one has to keep in mind that these measurements are from a reactor different from that in Stage 12 and 13, and that there are only two measurements available. In view of these circumstances, the results from this Stage are considered to be consistent with those of the previous Stages.

Fig. 4 shows the trend analysis of the frequencies of the two modes. For both Modes, the frequency is mostly unchanged, except for Mode 2 where several detectors indicate decreased frequencies. It is also seen that the mean values of, the frequencies are slightly different as compared to those of the previous Stages for both Modes. In Stages 12 and 13, the frequency of Mode 1 was in the range of 7 Hz, and in the present Stage, it is situated around 7.70 Hz. For Mode 2, in Stages 12 and 13 the frequency was around 8 Hz, whereas in the present case, it is around 8.70 Hz. The reason for this difference is that the first set refers to R4 and the second to R3. These two reactors are of identical construction, hence one should expect frequencies that are the same for the two cores. However, the core loading and the type of fuel used may be different for the two cores, which will affect the frequency of the individual fuel assembly vibrations in the first place, but possibly even that of the whole core barrel.

2.3. Conclusions, further work

The overall conclusion is that the results of the present analysis are compatible with the previous one and conform with the hypothesis formulated in Stage 12, but they do not yield a decisive proof. To obtain a thorough confirmation of the hypothesis, there is still a need for analysing three measurements, taken at BOC, MOC and EOC during one cycle. In view of the possibility of resolving the two beam mode peaks with high accuracy, it is advisable that the measurement is taken in R4.

3. AN INVESTIGATION OF THE ULTRA-LOW FREQUENCY OSCILLATIONS IN REACTOR POWER IN R3 AND R4

The motivation for these investigations is a general increase in the neutron noise amplitude level in R3 and R4, which leads to operational disturbances including certain alarms. More details on the background are given in the previous report, Stage 13 [14]. A preliminary study was made in Stage 13 which was not conclusive, and it was decided that another

Table 3.

Channel	Sensor
0	CET D3
1	CET E14
2	CET N4
3	CET M11
4	PRESSURE
5	CET J12
6	CET H8
7	Ex-core N41U AC
8	Ex-core N42U AC
9	Ex-core N43U AC
10	Ex-core N44U AC
11	Ex-core N41L AC
12	Ex-core N42L AC
13	Ex-core N43L AC
14	Ex-core N44L AC

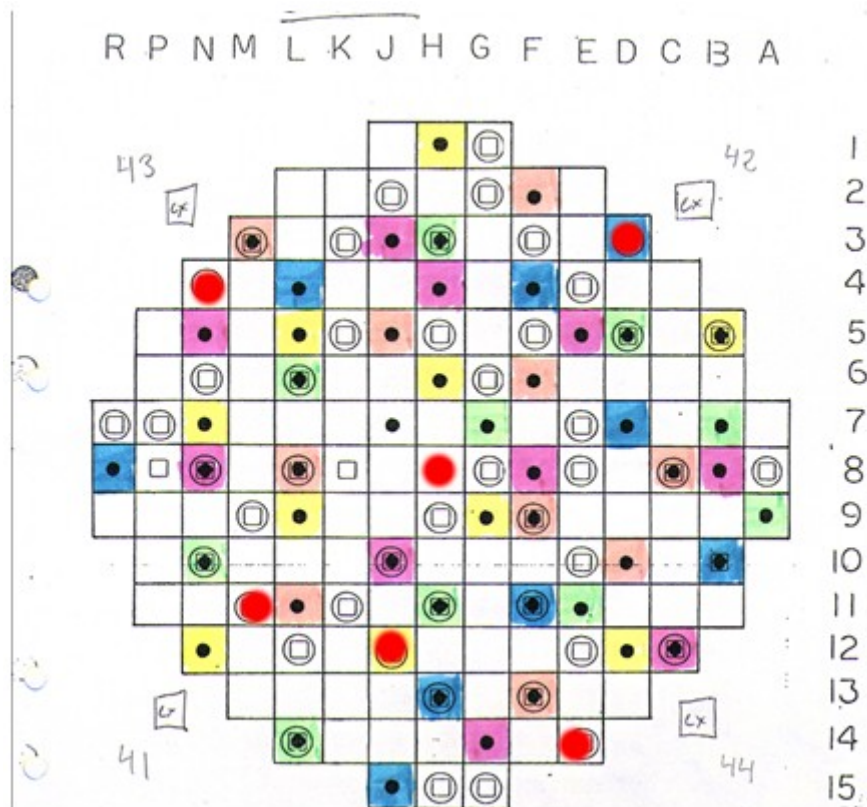


Fig. 5 Core map showing the radial positions of the in-core thermocouples (red circles) and the positions of the ex-core neutron detectors

attempt would be made in the present Stage. To this end, new measurements were made and analysed in order to understand the root cause of these oscillations. The measurements were taken in Ringhals-3 on 26/08/2010 from 11:33:44.193 to 17:33:44.193, using a 4 Hz sample rate. In Table 3 a list of the measured signals is given. More details of the measurement data are given in Ref. [18].

The positions of the in-core thermocouples, in relation to the ex-core neutron detectors, are shown in Fig. 5. Several pairs of thermocouple-neutron detectors were selected to perform the study. The pairs selected which are radially close were the following:

- N41-cetM11
- N41-cetJ12
- N42-cetD3
- N43-cetN4
- N44-cetE14

As the core map shows, one of the thermocouples is situated in the centre of the core. This was not included into the study since it is not close radially to any of the ex-core neutron detectors.

In the analysis of the measurements, two features were investigated. One of them was a cross-spectral and cross-correlation analysis of the selected ex-core detector – core exit thermocouple pairs. The motivation for this was firstly to show physical coupling between these signals. Earlier experience shows that the coolant flow in the downcomer, past the ex-core detectors and then upwards in the core up to the core exit thermocouples, establishes a common component in these two sensors due to the propagating temperature fluctuations which survive all the way long. Although this coupling is understandably weak, nevertheless it is sufficient such that the transit time of the coolant between the ex-core detectors and the core exit thermocouples, hence the coolant velocity, can be determined. Moreover, by selecting thermocouples close to the different ex-core detectors, the measurement gives a local value, which can be associated with the coolant flow in the respective quadrant of the core, closest to the ex-core detector. The significance is that in one case in the past, one could observe a tilted (asymmetric) radial distribution of the flow velocity, such that two quadrants had a slightly higher flow velocity than the other two. The interesting aspect is that the velocity distribution tilt itself showed an ultra low frequency oscillation, in that the role of the higher and lower velocity quadrants changed role with a very low frequency (far sub-Hz region) (Ref. [23]). To date, this is the only known physical process which can be associated with ultra low-frequency noise, and we wanted to test whether such a phenomenon takes place in the Ringhals 3 and 4 reactors, too. Hence, similarly to Stage 13, attempts were made to extract the flow velocity in the four quadrants of the core.

The second type of investigations concerned a bi-variate or multi-variate partial coherence analysis, also known as Signal Transmission Path Analysis (STPA) (Ref. [19]). The essence of STPA is that for signals being related through physical processes and hence their variations having a larger than zero coherence, it can point out which signal is the reason (source) and which is the consequence (the affected signal) in the fluctuations measured in the respective signals. Such an information helps to find the root cause of phenomena that are not well understood. To this end, STP analysis was performed for the

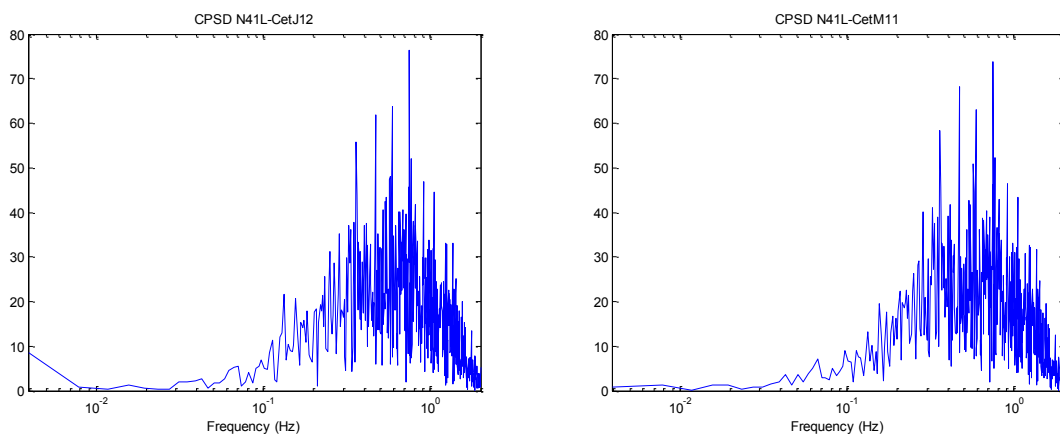


Fig. 6 Cross Power Spectral Density of the detector pairs N41L-CETM11 and N41L-CETJ12

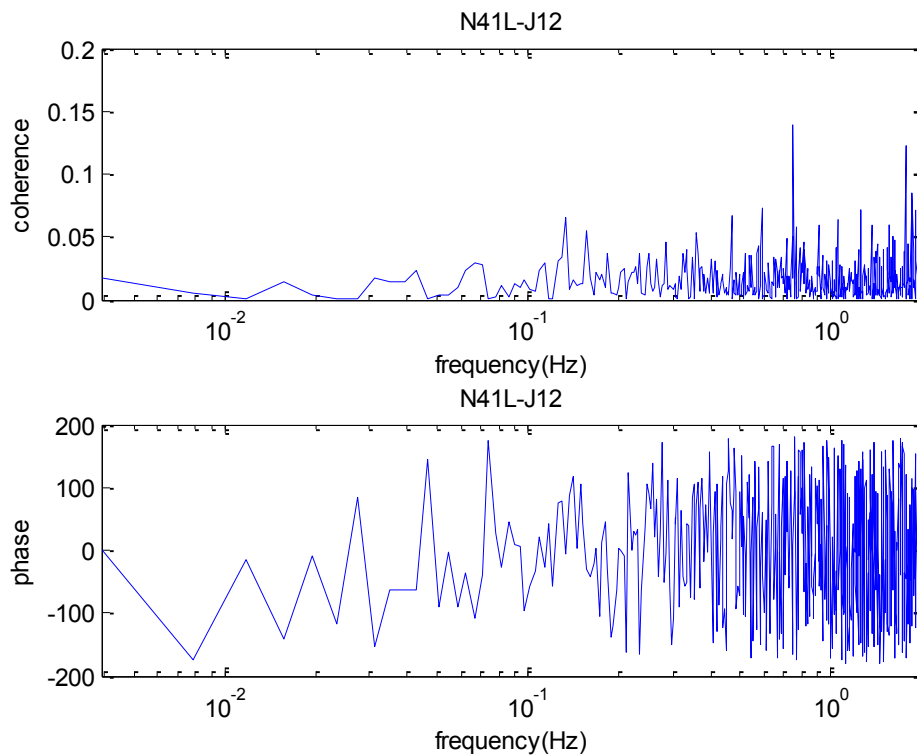


Fig. 7 Coherence and phase of the pair N41L-CETJ12

same pairs of ex-core neutron detectors – core exit thermocouples as in the attempt to determine the flow velocity, with a MATLAB-based software.

However, the analysis was just as much inconclusive as in the previous Stage. The coherence between the detector pairs was very low, and the phase of the cross-correlation function did not give any consistent, and physically interpretable transit times. The SPT analysis served partial coherences equal to close to zero for all signal combinations. A few illustrations for two selected signal pairs, in forms of the CPSD, coherence and phase are given in Figs. 6 - 8. It is seen that the CPSD is very low at low frequencies, and it has a maximum below 1 Hz. But at the interesting ultra-low frequencies, the CPSD is practically zero. The coherence is very close to zero throughout, and the phase does not have any linear (or even monotonic) behaviour.

The reason for these negative results was understood when a more detailed checking of the measurement conditions was made. The explanation lies in the structure of the data acquisition system. For noise analysis, in order to effectively use all bits of the A/D converter, the DC component of the signal is usually eliminated. In the past, this was made by applying an electronic offset to the signal before it was fed into the A/D converter. In order to know the DC component, which is necessary for normalizing the signal, this offset value had to be registered. In Ringhals a new signal acquisition system was introduced a few years ago. In this system the signals are split into two branches and fed into two A/D converters. One of them is high-pass filtered before connecting it to the A/D converter, and

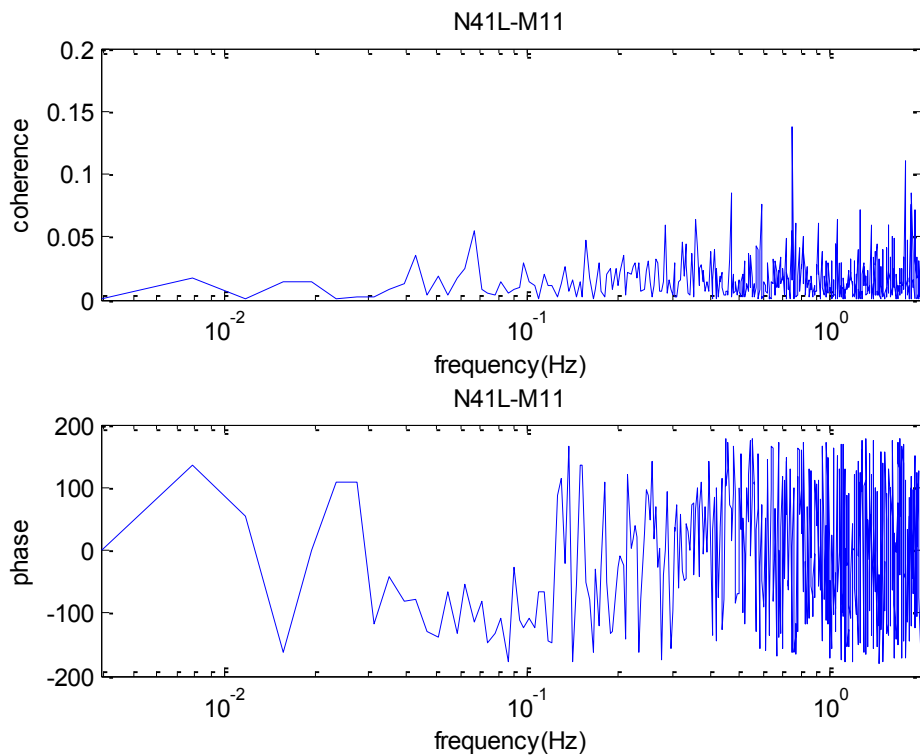


Fig. 8 Coherence and phase of the pair N41L-CETM11

this signal is free from the DC component. The result of the digitalization serves the noise signal for digital signal analysis. The other branch of the signal is not filtered, hence it contains the small fluctuations on top of a large mean value. This branch supplies the DC component of the signal after time averaging of the digitalized data.

It turns out that the break frequency of the high-pass filter is at 1.5 Hz, which means that all frequencies below 1.5 are filtered out from the AC component. This means that the AC component of the noise measurements at Ringhals is not suitable for the investigation of the ultra-low frequency oscillations. This explains the failure of the analysis in Stages 13 and 14.

The low frequency oscillations can presumably be studied from the so-called DC component. This is the component of the split signal which is not filtered. It contains the fluctuating part, but only as a small variation over a large DC component. Since the data acquisition hardware contains a 24-bit A/D converter, there is a chance that the fluctuating part of the signal can still be utilized for analysing the low frequency oscillations. This possibility will be explored in later Stages of the project.

4. FURTHER DEVELOPMENT OF THE THEORY AND SIMULATIONS TO DETERMINE VOID CONTENT IN R3 FROM THE ANALYSIS OF IN-CORE NEUTRON NOISE MEASUREMENTS

4.1. Introduction

As it was stated in the previous Stage 13, the determination of the void fraction in the core of BWR from in-core neutron noise measurements is not a trivial task and requires some sophisticated techniques to be developed to successfully perform it. Primarily, there are two conceptual methods out of several (both based on the analysis of the thermal neutron noise) which are worth to point out here and thus are discussed thereafter. The first one is based on the strong correlation between the so-called break frequency of the Auto Power Spectral Density (APSD) (Ref. [24]) of the measured noise and the void content at a corresponding axial core level (Ref. [27]). Another method refers to the estimation of the transit times for the void fluctuations to propagate between two different detector positions by calculating the Cross Power Spectral Density (CPSD) of the induced neutron noise. If one assumes a simple direct relationship between void fraction and two-phase flow velocity, then measuring the latter in the detector position, the void fraction can be determined. Unfortunately, due to several reasons none of the methods can be directly tested on actual power plant measurements. The difficulty with the first method is related to the fact that the corresponding measured neutron noise is usually filtered and all the frequencies above 16 Hz are suppressed. In practice, the break frequency usually ranges between 10-30 Hz, which makes its proper estimation from the current measurements quite complicated and almost impossible. As for the second method where the vapour velocity is first calculated from averaged void velocity and thereafter the void content is reconstructed, the precise estimation of the transit times is required to provide satisfactory results. An alternative way might be to use the increased number of detector measurements compared to the four ones which are available now.

In order to test both methodologies it is instructive to construct a simple model of the boiling process occurring in a real BWR heated channel (one fuel assembly) and then to simulate the corresponding induced neutron noise. Such a task is the main objective of the present stage. The model is based on the Monte Carlo technique (Refs. [28]-[30]) where the bubbles are generated randomly in both space and time. This approach has already been successfully tested in some earlier neutron noise application such as the modelling of a vibrating control rod or a fuel assembly (Refs. [24]-[26]).

The main advantage of this type of model is that, in addition to the simulated neutron noise signals, one has access to the original void and velocity profiles as these constitute model inputs. This provides an exclusive possibility to test the method of determining the void fraction and steam velocity from the neutron noise by comparing two sets of data. Another benefit from using this model is its applicability to the non-stationary processes which is a common assumption in traditional methods.

To this end, the description of the Monte Carlo model is given first and the corresponding techniques for the void fraction determination are followed thereafter. Finally, the results of the numerical simulation as well as the application of above-mentioned methods are discussed.

4.2. Model construction

In order to set up a realistic model for the two-phase flow using a Monte Carlo technique, a proper distribution for bubble generation should be found (Ref. [30]). As mentioned earlier, from the conceptual point-of-view the birth process of the bubbles should be generated by random sampling methods both in space and time. In the radial direction the distribution can be taken as homogeneous, whereas the axial distribution of bubbles should follow the behaviour of the actual BWR void profile. Hence, as a first approximation, it is intuitively reasonable to generate bubbles according to the spatial derivative of the axial void fraction $\alpha(z)$ as:

$$p(z) = \frac{d\alpha(z)}{dz} \quad (4)$$

where the latter quantity can be interpreted as a bubble generation rate per unit length between z and $z+dz$. However, in real Monte Carlo sampling one needs to use the cumulative probability function $P(z)$ rather than the explicit probability distribution $p(z)$. The former is usually defined as:

$$P(z) = \int_0^z p(z') dz' \quad (5)$$

with the cumulative probability function $P(z)$ giving the total number of bubbles generated between 0 and z . As a result, in our case the sampling function (the cumulative probability function) is chosen as the axial void fraction profile $\alpha(z)$.

In the general case, the axial void profile can be determined by constructing a simple model of the boiling phenomenon based on its analogy with the neutron diffusion theory. Similar to the neutron transport, which is usually described by diffusion equations representing the balance between neutron production and neutron leakage, the boiling process can be represented as a composition between two competing mechanisms. The first mechanism is associated with the production of the void due to the heating source located inside the BWR channel. Another mechanism, which also influences the void distribution, refers to the vapour transport within a channel due to a pressure drop between the inlet and the outlet of the core. Obviously, for certain values of system parameters, the competition between these two processes will lead to a proper void distribution.

In order to be strict from the thermal-hydraulic point of view, Eq. (4) should be actually written for the quality instead of the void fraction. However, to avoid additional complexity, in the present model a simpler case is considered where the bubbles are generated according to the static neutron flux (sin-function shape) as:

$$p(z) = \frac{\pi}{2H} \sin\left(\frac{z\pi}{H}\right) \quad (6)$$

and are allowed to propagate upwards with a certain velocity profile $v(z)$, where H denotes the height of the channel. In order to fulfil the general definition of probability $p(z)$ was normalized to unity. The form of Eq. (6) also assumes that one disregards the feedback of the void profile to the flux shape, which is obviously a simplification, but it still leads to realistic results.

Combining Eqs. (5) and (6), the cumulative distribution function $P(z)$ can be written as:

$$P(z) = \frac{1}{2} \left(1 - \cos\left(\frac{\pi z}{H}\right)\right) \quad (7)$$

whereby Eq. (7) constitutes the sampling function for the bubble generation in the present Monte Carlo model.

The axial velocity profile of bubbles can easily be estimated from the following steady-state mass conservation equation written for the mixture density between the vapour and the liquid phases of the coolant as:

$$\frac{\partial \rho_m(z) * v_m(z)}{\partial z} = 0 \quad (8)$$

Then, one gets for the axial bubble velocity:

$$v(z) = v_m(z) \approx \frac{v_0}{1 - \alpha(z)} \quad (9)$$

where $v_0 = v_l$ is the velocity of the liquid phase at the channel inlet. In the last equation the second term in the denominator is neglected due to its smallness. Although Eq. (9) is somewhat peculiar from the mathematical point of view (since it becomes singular when the void fraction reaches unity), it is still applicable for the current Monte Carlo simulation where a void fraction profile is kept close to the real BWR one which is usually below 0.8.

4.3. Principles of the simulation

As a starting point, a two-dimensional model of the heated channel, representing a cross-section of a real fuel assembly is chosen. Only one dimension is assumed for the radial direction, denoted by x , and the axial direction, in which the two-phase flow is propagating, is denoted by z . The bubbles are represented as 2-D circles in this model. The coordinates of the bubble centres are generated by random sampling methods along the x and z dimensions. As mentioned earlier, the sampling of bubbles in the z -direction is performed in such a way that the mean void fraction corresponds to that of a real BWR, whereas, without loss of generality, the sampling in the x direction is taken as a uniform one.

From the conceptual point-of-view, it is important to underline that the overlapping between different bubbles is not allowed in the present model. The bubble diameter is set to $d_{bubble} = 0.8$ cm while the diameter of the heated channel is chosen equal to the typical BWR one $D = 20$ cm. The height of the channel corresponds to the length of a BWR fuel assembly, i.e. to $H = 400$ cm. The bubble inlet velocity is taken to be $v_0 = 200$ cm/s corresponding to a typical inlet flow BWR velocity under normal operational conditions. To provide proper detection intensity and time resolution, the time step in the data processing is selected equal to $\delta t = \frac{d_{bubble}}{5v_0} = 0.0008$ seconds which gives an opportunity to detect the same bubble up to 5 times while it bypasses the detector aperture.

The simulation starts with generating 100 bubbles at $t = 0$ s and proceeds with random injection of 35 new bubbles at each consecutive time step. Since the transient part of the simulation is not of interest here, the recording of calculated void fluctuations as well as the corresponding induced neutron noise is started after 20 seconds of the simulation and thus eliminates any transient effects. The total simulation time is limited to $T_{sim} = 520$ seconds, which was chosen to be equal to the time duration of a measurement made in Ringhals-1, which will be used at a later stage of the project for testing the method. In order to facilitate the void calculations, the entire 2D ZX-plane of the heated channel is divided into horizontal layers, each of size $\delta z = 0.1$ cm. The void fraction is then estimated for each axial position between the layers and for each time step by calculating the total intersection length between the bubbles and the corresponding layer boundary. In order to evaluate the void fraction, the total intersection length of bubble crossings for each axial level is weighted with the heated channel diameter D . It has to be noted here that, for the real application of the model, the void fraction should not exceed the critical value corresponding to the void fraction limit for the bubbly flow regime. The latter means that the bubble generation rate should be properly chosen in order to satisfy the above-mentioned condition. However, for the better visibility of the methodology, the void fraction in the current model is somewhat higher than the ordinary one for the bubbly flow. Moreover, for the higher void fraction ($\alpha > 0.5$) one can not really consider the bubbles as a fluctuating part inducing the variations in the neutron flux since both the liquid and vapour particles are equally likely to be registered.

Likewise, the axial velocity $v(z)$ is also calculated for each axial position separately via Eq. (9). It is worth mentioning, that the real bubble velocity is usually a continuous function in space. However, due to spatial discretization, the velocity in the present model is evaluated only in a discrete number of spatial points. Furthermore, due to the random character of bubble production, and in addition owing to the fact that the bubbles are born instantaneously with full size, the axial velocity also becomes a random quantity, which also incurs that some bubbles at lower axial elevations can move faster than those with a higher axial position, which is unrealistic. In addition, some of the bubbles may get overlapped by this “catching up” effect, whereas overlapping is not allowed in our model.

To tackle the above-mentioned problem, the velocity profile is fitted with a third order polynomial function just after the system reaches a steady state. Obviously, in such a case the velocity becomes a continuous function in space.

4.4. Determination of the void content: methods

In this section a short summary of two existing methods for estimating a void content from neutron noise measurements is given. The first method has its origins in the late 70s and is based on the correlation between the so-called break frequency of the Auto Power Spectral Density (APSD) of the measured neutron noise, and the corresponding axial positions of detectors (Ref. [27]-[30], [31]). Another way of correlating neutron noise with the void content is to use the relationship between void fraction and void velocity, as is shown in Eq. (9). By virtue of such a monotonic relationship, determination of the void fraction would be reduced to that of the void velocity. The void velocity can be determined from measurement of the transit times of the propagating density (void) fluctuations between pairs of in-core detectors in the same radial position, estimated from the Cross Power Spectral density (CPSD) between the detectors. Reconstruction of the velocity from a few measured transit times is, however, by far not trivial, and it requires the elaboration of some unfolding methods and algorithms. Below a cursory overview of those two approaches will be given, without going into detailed descriptions.

4.4.1. APSD break-frequency approach

As is customary in noise diagnostics for the interpretation of neutron noise measurements in a large power system, it is instructive to separate the total system response into two specific components, the so-called global and local components (Ref. [24]). The existence of both components can be easily shown by solving two-group diffusion equations written for the time-space dependent neutron noise. In such a case the characteristic equation has two distinct roots corresponding to two different solutions, the λ -solution and the μ -solution. The first one can be directly related to the local component of the neutron noise mentioned above whereas the global component is usually generalized as a μ -term. The appearance of two different components in case of two group diffusion theory is the consequence of two characteristic processes that neutrons undergo during their life-time, namely the slowing down with an apparently large relaxation length and the diffusion itself with quite a small relaxation distance. As a result, the local component obviously describes the noise distribution locally (only in the vicinity of the perturbation), while the μ -component characterizes the behaviour of the neutron noise over the entire system. In addition, from a physical point-of-view, it is reasonable to associate the local component with a high-frequency content of the neutron noise when the system does not have enough time to respond globally to the corresponding local perturbation but rather in the neighbourhood of the source. In this case, the global component will thus reproduce the rest or low-frequency component of the neutron noise.

From a diagnostic point-of-view, the local component is of the largest practical importance, especially for a BWR where it is usually employed for describing local density fluctuations in the vicinity of a detector position. For this reason, the high-frequency component of the APSD of measured neutron noise is of major interest in cases where two-phase flow fluctuations are analyzed. Taking into account the correlation between the local component and the corresponding propagating density variations, assuming that there are no other noise sources present in the system, the following simplified relation between the normalized Auto Power Spectral Density (NAPSD) of density fluctuations and the one corresponding to the induced neutron noise can be derived [27]:

$$NAPSD_z^{\delta\phi_\lambda} = C * NAPSD_z^{\delta\alpha}(\omega) * \frac{1}{(1 + \omega^2 \tau_\lambda^2)^2} \quad (10)$$

where $\tau_\lambda(z) = v(z) * \lambda(z)$, $v(z)$ is the axial velocity of void fluctuations and $\lambda(z)$ is the spatial decay constant of the local component at the axial elevation z .

From Eq. (10) it is clearly seen that the fluctuations in the neutron flux $\delta\phi_\lambda$ at a certain axial position z are proportional to the corresponding fluctuations in the void fraction $\delta\alpha$ at the same location z times the Lorentzian coefficient. Such a straightforward correlation is not surprising and becomes obvious if one takes into account the local character of density perturbations themselves. Due to the decaying behaviour of the Lorentzian term in Eq. (10), the term acts as a low bandpass filter for the corresponding neutron field with a break frequency. Thus, from Eq. (10), the break frequency of the APSD of the neutron noise can be defined as [27]:

$$f_b(z) = \frac{1}{2\pi} v(z) * \lambda(z) \quad (11)$$

As is clearly seen from Eq. (10), the decreasing behaviour of the Lorentzian term with increasing frequency leads to the decreasing contribution of density fluctuations into the total response. In fact, this means that the break frequency is capable of characterizing the contribution of two-phase flow fluctuations into the neutron noise. Above this frequency the contribution of void fluctuations can be assumed to be negligible compared to other types of neutron noise sources which might become dominant. At the same time, the break frequency can be interpreted as the registration rate of the bubbles passing through the detector, namely the higher the velocity of bubbles, the higher the break frequency. At this point the relationship between void fraction and break frequency is implicit, and it is embedded into the dependence of both the velocity and the spatial decay constant on the void fraction. Thus, in principle, the break frequency can characterize the level of void fraction at the corresponding axial level. However, one also has to take into account that the increasing void fraction leads not only to the increase of the bubble velocity, but also to a decrease of the spatial decay constant λ of the local component. The aggregate effect is therefore a more complicated function of the void fraction than it may seem at the first sight. As a result, the break frequency dependence on the void fraction is defined by two

mechanisms: bubble velocity and the size of the local component. Both effects are taken into account while the modelling is performed.

In practice, the ASPD of the neutron noise can easily be calculated from measurement data which means that for the proper sampling frequency, the break frequency can be estimated and thereafter correlated to the void fraction. For the completion of the method, the explicit relation between the local component and the void fraction is derived below.

Assuming that the detector is located in the coolant region, for the local component one obtains [24], [27]:

$$\lambda = \sqrt{\frac{1}{L^2} + \frac{1}{\tau}} \approx \frac{1}{L} = \sqrt{\frac{\Sigma_{a2}}{D_2}} = \sqrt{3\Sigma_{a2}\Sigma_{tr2}} \quad (12)$$

where L^2 and τ denote the thermal diffusion and slowing down areas, respectively, Σ_{a2} is the thermal absorption cross section, D_2 is the thermal diffusion coefficient and $\Sigma_{tr,2}$ is the transport cross section. Assuming the following approximation for both the absorption and transport cross sections:

$$\Sigma_{a2,tr2} \approx a_{1,2}(1 - b_{1,2}\alpha(z)) \quad (13)$$

where $\alpha(z)$ is the axially dependent void fraction, and combining the last equality with Eqs. (12)-(13), applying a Taylor expansion ($b_1, b_2 < 1$) and neglecting the second order terms, one gets for the local component:

$$\lambda = \lambda_0 - k * \alpha(z) \quad (14)$$

where $\lambda_0 = \sqrt{3 * a_1 * a_2}$ and $k = \frac{b_1 + b_2}{2} * \lambda_0$. Finally, combining Eqs. (9), (11) and (14) for the axial void fraction yields:

$$\alpha(z) = \frac{u - 1}{u - k} \quad (15)$$

In the above, $u = \frac{v_0 \lambda_0}{2 * \pi * f_b(z)}$, $f_b(z)$ is the break frequency calculated from the noise measurements (in our case from Monte Carlo simulations), v_0 is given as the inlet velocity and λ_0 is the local component at the channel inlet. The last parameter λ_0 together with k , both characterizing the local component, can be easily estimated by combining Eq. (14) together with CASMO calculations. Namely, performing a number of CASMO runs for a single BWR fuel bundle with different void content, the dependence of the two-group cross sections on the averaged void fraction can be determined. Since in the two-group approach the dependence of the local component on cross sections is given in a simple analytic form, the correlation between the local component and void fraction becomes straight forward. Fitting this correlation to Eq. (14) will provide the numerical values for both λ_0 and k .

4.4.2. Transit time approach

The second method of estimating the void fraction from neutron noise measurements is computationally less expensive. It is based on the assumption that the local two-phase flow velocity can be determined from the transit times of the density fluctuations between different detectors pairs, and hence it only requires the knowledge of the transit times. As is well-known in noise diagnostics, the transit times can be evaluated from the CPSD calculated for two detectors located in the same radial but different axial positions (Ref. [24]). In the general case, the CPSD can be written as:

$$CPSD_{\delta\phi_z}(z_i, z_j, \omega) = APSD_{\delta\phi_z}(z_i, \omega) * \exp(-i\omega\tau_{ij}) \quad (16)$$

where τ_{ij} is the transit time of propagating density perturbations (i.e. upwards-propagating bubbles) defined as:

$$\tau_{ij} = \frac{z_j - z_i}{v_{ij}}, \quad (17)$$

with z_i and z_j standing for the axial positions of two detectors and v_{ij} is the average propagating velocity of bubbles between two consecutive detectors. Usually, $APSD_{\delta\phi}(z, \omega)$ is assumed to be frequency independent over the frequency region of interest, and depends only on the axial position (elevation) z .

From Eq. (16) it is clearly seen that the corresponding transit times can be determined from the phase of the CPSD function. However, for reasons of simplicity, in the present calculations, the transit times were estimated from the Cross-Correlation Function (CCF) which can be calculated from the inverse Fourier transform of the CPSD.

The main problem with this method is that the relationship between the transit times and the local velocity is rather implicit and has an integral form. The transit time between two axial points z_1 and z_2 is related to the local velocity $v(z)$ as

$$\tau_{ij} = \int_{z_i}^{z_j} \frac{dz}{v(z)} \quad (18)$$

where $v(z)$ is the axial bubble velocity. To reconstruct the velocity profile from a few values of the transit times requires an assumption for the analytical form of the velocity profile, which has as many unknown parameters as the number of measured transit times, and then construct an “unfolding procedure” to extract those parameters from the known discrete transit times.

In the Swedish BWRs there are four detectors axially in each radial detector position (also referred to as a detector string), which supply three independent discrete transit times. To reconstruct the velocity profile from three measured transit time values is not a trivial task, hence we will assume a fifth detector (such as a TIP), and assume to have access to four transit time values. Due to the inflexion point of the velocity profile, the simplest

assumption is to approximate it with a 3rd order polynomial function, containing 4 coefficients, as:

$$v(z) = az^3 + bz^2 + cz + d \quad (19)$$

Using the measured transit times for 4 different detector pairs and taking into account Eq. (19) the following system of equations for identifying the unknown coefficients a , b , c and d can be given:

$$\int_{z_i}^{z_{i+1}} \frac{dz'}{az'^3 + bz'^2 + cz' + d} = \tau_{i,i+1} \quad (20)$$

where $i = 1, 2, 3, 4$. Once the unknown coefficients are determined by e.g. a parameter fitting procedure, the axial velocity profile can be reconstructed, and hence, the void profile can be calculated from Eq. (9).

This method is advantageous from the practical point of view since it does not require any extra data other than noise measurements. On the other hand, the transit times should be estimated in a quite precise way, or an increased number of detectors should be used. Moreover, the direct application of the 3rd order approximation described above, has an additional drawback. It is the fact that the determination of unknown coefficients in Eq.(19) requires the direct integration of the inverse velocity as well as to solve the set of nonlinear equations (20). From the mathematical point of view such a task can be complicated and ambiguous (many-valued).

Thus, from the practical point of view, it is more instructive to apply a different approximation: namely to assume a piecewise construction of the assumed form of the velocity profile curve into several regions (two or three, as we will do in the forthcoming) and fit each part to a second or first order polynomial. The corresponding approximation for subdivision into two curves can be written as:

$$v(z) = \begin{cases} a_1 z^2 + b_1 z + c_1 & \text{if } z < z_0, \\ a_2 z^2 + b_2 z + c_2 & \text{if } z \geq z_0. \end{cases} \quad (21)$$

For the convenience of consideration, we assign the following detector positions z_1 , z_2 , z_5 and z_6 to the LPRM detector and assume that the TIP detector, supplying the fifth measurement, is placed between the second and the fifth LPRM (i.e. fixed detector in the string), and it will be designated by z_4 . It should be noticed that the third detector z_3 is excluded from our consideration as irrelevant since it is only assumed five detector measurements available. The division point z_0 of the two profiles will lie between z_2 and z_4 . Then, by taking also into account the difference in the distances between the various detectors and the position of the division point between the two profiles, the unknown coefficients a_1 , b_1 , c_1 , a_2 , b_2 , c_2 can be estimated from the following conditions:

- first profile:

$$\begin{cases} \tau_{12} = \int_{z_1}^{z_2} \frac{dz'}{a_1 z'^2 + b_1 z' + c_1}, \\ \tau_{23} = \int_{z_2}^{z_3} \frac{dz'}{a_1 z'^2 + b_1 z' + c_1}, \\ v(z)|_{z=0} = v_0. \end{cases} \quad (22)$$

- second profile:

$$\begin{cases} a_1 z_0^2 + b_1 z_0 + c_2 = a_2 z_0^2 + b_2 z_0 + c_2, \\ 2a_1 z_0 + b_1 = 2a_2 z_0 + b_2, \\ \tau_{56} = \int_{z_5}^{z_6} \frac{dz'}{a_2 z'^2 + b_2 z' + c_2}, \end{cases} \quad (23)$$

where v_0 is the channel inlet velocity. The first and second equalities in Eq. (23) constitute the continuity of the void velocity and its derivative in the point z_0 . In principle, the last condition in Eq. (23) can be replaced with some other transit time condition, for example one containing z_0 or τ . The only requirement for such a case is that the transit time should correspond to the correct region of the velocity profile. The parameter z_0 can be chosen arbitrary but located in the linear region of the velocity profile. Moreover, if the inlet coolant velocity is not known, it can be replaced with the condition of zero velocity derivative at $z = 0$, namely with the following relation:

$$\left. \frac{dv(z)}{dz} \right|_{z=0} = b_1 = 0. \quad (24)$$

Due to the arbitrariness of the value of z_0 , approximation (21) is not self-consistent. For this reason, it is more reasonable to divide the void velocity profile into 3 parts instead of two as it is shown above. Thus, one gets for the axial velocity profile:

$$v(z) = \begin{cases} a_1 z^2 + b_1 z + c_1, & \text{if } z < z_{01} \\ a_2 z + b_2, & \text{if } z_{01} \leq z \leq z_{02} \\ a_3 z^2 + b_3 z + c_3, & \text{if } z > z_{02}. \end{cases} \quad (25)$$

The corresponding conditions for determining $a_1, b_1, c_1, a_2, b_2, a_3, b_3, c_3$ can be written as:

- first profile:

$$\begin{cases} \tau_{12} = \int_{z_1}^{z_2} \frac{dz'}{a_1 z'^2 + b_1 z' + c_1}, \\ \tau_{24} = \int_{z_2}^{z_4} \frac{dz'}{a_1 z'^2 + b_1 z' + c_1}, \\ v(z)|_{z=0} = v_0. \end{cases} \quad (26)$$

- second profile:

$$\begin{cases} a_1 z_{01}^2 + b_1 z_{01} + c_2 = a_2 z_{01} + b_2, \\ 2a_1 z_{01} + b_1 = a_2, \\ \tau_{24} = \int_{z_2}^{z_4} \frac{dz'}{a_2 z' + b_2}. \end{cases} \quad (27)$$

- third profile:

$$\begin{cases} a_3 z_{02}^2 + b_3 z_{02} + c_3 = a_2 z_{02} + b_2, \\ 2a_3 z_{02} + b_3 = a_2, \\ \tau_{45} = \int_{z_4}^{z_5} \frac{dz'}{a_3 z'^2 + b_3 z' + c_3}, \\ \tau_{56} = \int_{z_5}^{z_6} \frac{dz'}{a_3 z'^2 + b_3 z' + c_3}. \end{cases} \quad (28)$$

where in Eqs. (27) and(28), the first and second equations are based on the continuity of the void velocity and its derivative. Compared to the previous method the difference is that the two interface points z_{01} and z_{02} between the three profiles are kept as unknowns, and are also determined from the corresponding conditions (27)-(28). Then the corresponding velocity profile can be defined as a piecewise function via Eqs. (21) and (25).

In the next Section, the corresponding parameters for both methods are calculated from the simulated neutron noise measurements, provided by the Monte Carlo model.

4.5. Simulation results

A large number of simulations of the bubbly flow, and subsequent calculations of the induced neutron noise as well as velocity and void fraction profile reconstructions have been performed. Out of these only some characteristic results will be presented below. As a starting point, 520-second long void fraction signals are generated by the Monte Carlo two-phase flow model. When simulating the induced neutron noise, these were performed at six different axial levels at the same radial position. This was made mostly for testing purposes; in the work with the reconstruction of the velocity and void fraction profile, only

five detectors were used, corresponding to the experiments. The detector locations are given in the first column of Table 4 below. For the convenience of calculations, void fraction signals were recorded in a binary form where "1" indicates the presence of a vapour bubble in the detection point, and "0" designates the presence of water in the position in question. The detection of vapour bubbles is controlled by estimating the distance between a bubble centre and a detector. The corresponding normalized neutron noise is generated through the spatial convolution between the void fraction signals and the local component of the transfer function as

$$\frac{\delta\phi_\lambda(t, z)}{\phi(z)} = \int_0^H \exp(-\lambda(z)|z - z'|) \delta\alpha(t, z') dz' \quad (29)$$

where $\delta\phi_\lambda(t, z)$ denotes the local component of the neutron noise due to void fraction fluctuations, $\delta\alpha(t, z')$ is the fluctuation of the simulated void fraction signal at axial position z' and $\lambda(z)$ is the axially-dependent local component calculated from CASMO. As an illustration, one such neutron noise signal is shown in Fig. 9 in two different time scales.

Subsequently, the power spectral densities for each of the six detectors are calculated by using standard FFT. The results are given in Fig. 10. It can be seen from this figure that the break frequency of the APSD strongly depends on the axial position of the detector and monotonically increases with the increasing axial elevation. Intuitively, such a dependence can be explained by a higher void content at the higher parts of the heated channel and consequently by higher propagating velocity, as it was mentioned previously.

Table 4 Results of the curve fitting procedure of APSD for the Monte Carlo simulated neutron noise to the Lorentzian coefficient (Eq. (10)).

Detector position, z_d [cm]	Amplitude, A [a.u.]	τ_λ , [s]	Break frequency, f_b , [Hz]
$z_1 = 20$ cm	$1.54 \cdot 10^6$	0.064	15.62
$z_2 = 60$ cm	$9.73 \cdot 10^6$	0.063	15.87
$z_3 = 100$ cm	$1.53 \cdot 10^7$	0.056	17.86
$z_4 = 130$ cm	$1.67 \cdot 10^7$	0.052	19.23
$z_5 = 240$ cm	$1.38 \cdot 10^7$	0.039	25.64
$z_6 = 360$ cm	$1.38 \cdot 10^7$	0.039	25.64

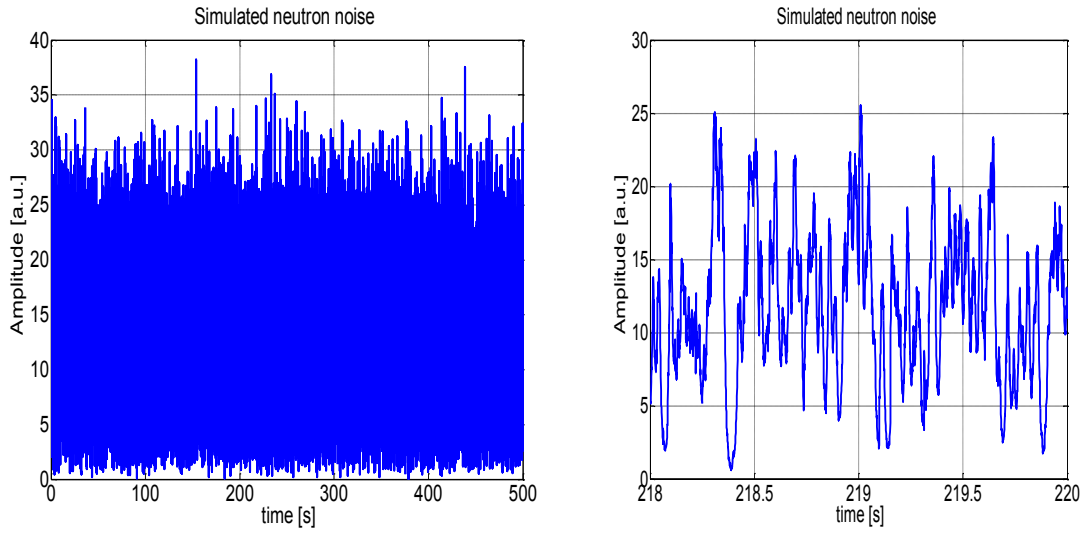


Fig. 9 Time dependence of the neutron noise induced by the two-phase flow fluctuations as calculated from the Monte Carlo model.

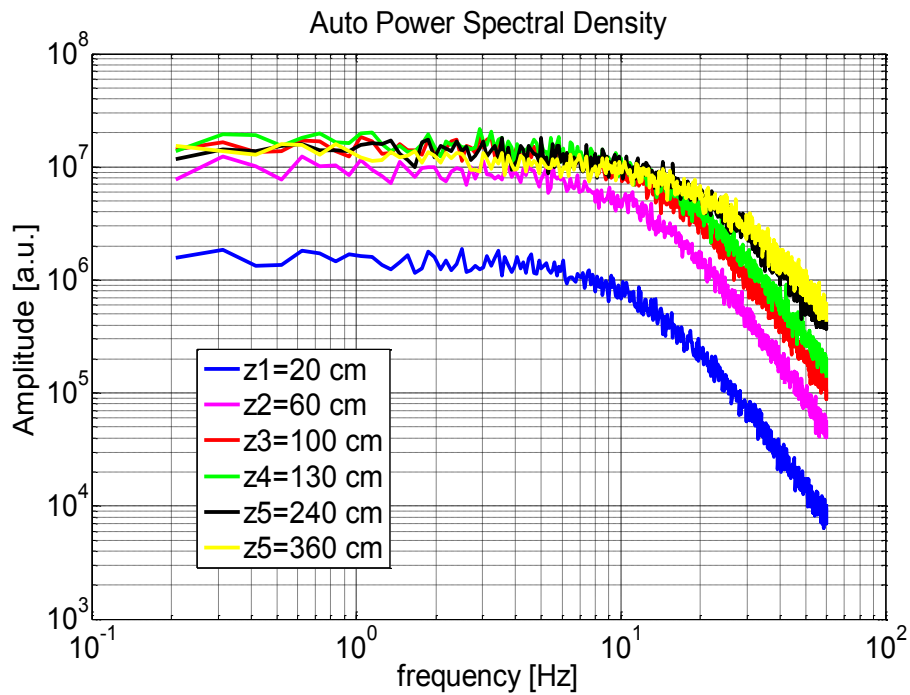


Fig. 10 Normalized Auto Power Spectral Densities of the simulated in-core detector signals calculated for four axial elevations $z_d=20, 60, 100, 130, 240, 360$ cm, respectively.

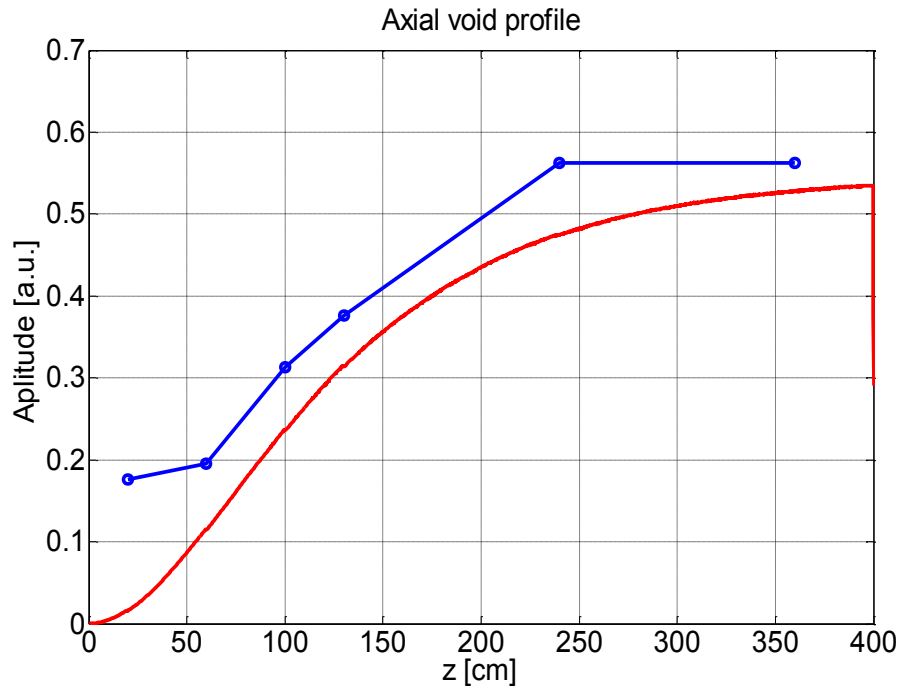


Fig. 11 Reconstructed (“experimental”) axial void profile as calculated by the break frequency method (Eq. (15)) (blue line) and “true” axial void profile (red line).

As a result, the impact of density fluctuations on the total neutron noise in the upper part of the core manifests itself in the expansion of the plateau region of the APSD. Likewise, the amplitude of the APSD for the first four cases also increases with increasing axial position. One possible reason for such a behaviour of the APSD, as one can see from Eq. (10), might be due to the higher void fraction fluctuations in the upper part of the heated channel. However, this is not the case for the last two points $z = 240$ cm and $z = 360$ cm where the void content is around 0.5 and the vapour bubbles can not be considered as a fluctuation with respect to the liquid phase.

The break frequencies for all six APSDs as well as their amplitudes were numerically estimated by fitting the corresponding curves to the Lorentzian coefficient defined in Eq. (10) (see Table 4). This procedure also gives the transit time τ of the void through the range of the local component, by using the quantitative values of λ . These are also given in Table 4.

As a next step, the estimated break frequencies are substituted into Eq. (15) to recalculate the void fraction in the six detector locations. The result is plotted in Fig. 11 (blue line). For comparison, the “true” void profile (calculated by time averaging over the corresponding set of simulated void fraction signals) is also shown in Fig. 11 with a red line. From the two figures, one can conclude that the void fraction calculated from the simulation qualitatively reproduces the behaviour of the “true” one. However, the break frequency method slightly overestimates the void fraction, primarily in the lower part of

Table 5 Results of the transit time calculations from the Monte Carlo simulation (both “true” and “experimental”)

Detector distances, d_{ij} , [cm]	τ_{tr} , [s] (Eq. (18))	τ_{exp} , [s] (CCF)	v_{tr} , [cm/s]	v_{exp} , [cm/s]
$z_{12} = 40$ cm	0.19	0.19	210	210
$z_{23} = 40$ cm	0.16	0.16	250	250
$z_{34} = 30$ cm	0.11	0.10	273	273
$z_{45} = 110$ cm	0.32	0.29	344	380
$z_{56} = 120$ cm	0.29	0.24	414	500

the channel. From the practical point of view this region is less interesting since it usually corresponds to the subcooling area where the void fraction is low.

Next, the results for the second method are discussed. The CCF between different detector pairs is estimated using the detector signals generated by the Monte Carlo model. Then, the corresponding transit times τ_{exp} (further called “experimental transit times”) and averaged velocities v_{exp} (further called “experimental” averaged velocities) are calculated and the results are given in Table 5.

For sake of comparison, the transit times τ_{tr} (further called “true” transit times) between the detector pairs are calculated from the “true” velocity profile (see Fig. 12) and the corresponding averaged velocities v_{tr} (further called “true” averaged velocities) between different detectors are given in the last two columns in Table 5. As one can note, the results from the two methods are in a good agreement with each other except for the last case where the difference between the estimation methods becomes significant. This inconsistency between the two methods is probably due to the less correlated behaviour of the simulated bubbly flow in the upper part of the core where the size of the local component is higher compared to the one in the lower part. Moreover, this part of the core is less relevant, since in reality the high void fraction level does not correspond to a bubbly flow regime, which is the only regime simulated here. Once the transit times are found, one can estimate the unknown coefficients for the velocity profile (see Eq. (19)) as it was mentioned in the previous Section.

As it was stated in the previous section, from the practical point of view it is more reasonable to approximate the velocity profile with a piecewise function rather than directly with the third order polynomial. The results of axial velocity profile

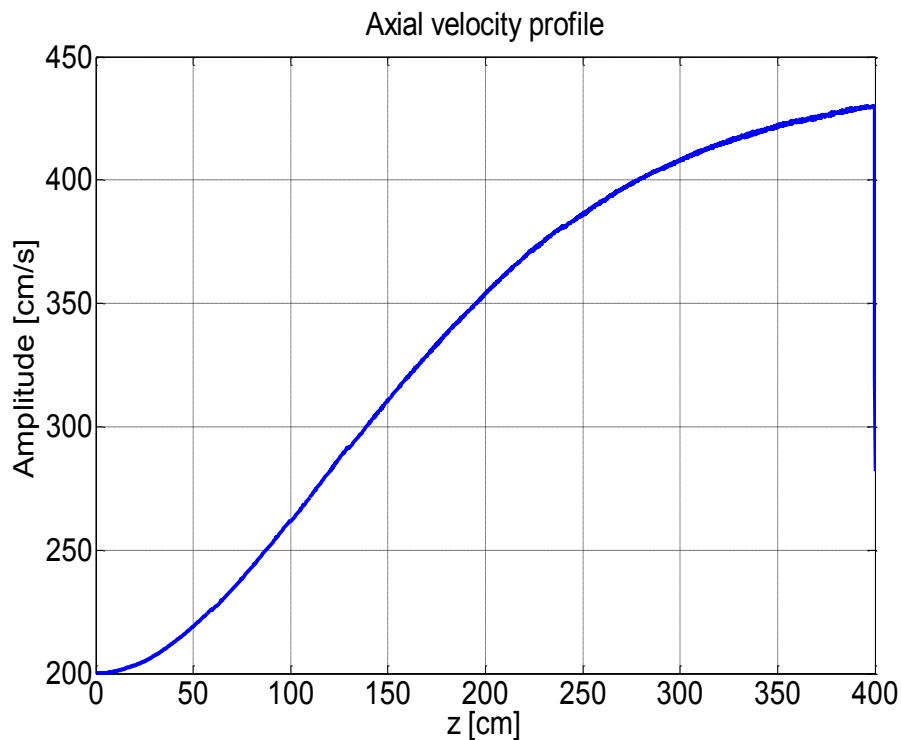


Fig. 12 “True” axial velocity profile as calculated from Eq. (9)).

reconstructions using piecewise approximations (21) and (25) are shown in Figs. 13 - 14 and Figs. 15 - 16, respectively.

Fig. 13 shows the case when the axial void velocity profile is reconstructed by applying approximation Eq. (21) combined with conditions (22)-(23) and designated correspondingly as “Method 1”. For comparison, in Fig. 14 the results for same method (based on Eq. (21)) are given, but the zero inlet velocity condition (second equation in Eq. (22)) is replaced with zero inlet velocity derivative condition (Eq. (24)). This method is denoted as “Method 2”. Fig. 15 corresponds to the case when the more sophisticated approximation (25) is applied with corresponding conditions given by Eqs. (26), (27) and (28). This method is called “Method 3”. Similarly to the previous case, in Fig. 16 the result for the same method, “Method 3” with the replaced zero inlet velocity condition by zero inlet velocity derivative condition (see Eq. (24)) is shown (designated as “Method 4”).

From these figures one can conclude that all four methods supply very similar, nearly identical results. This means that the fact whether a two- or three-region piecewise representation, and whether zero velocity value or zero spatial derivative of the velocity is used at the inlet as a boundary condition, has little influence on the results. In all cases, the velocity profile reconstructed from the simulations overestimates the “true” one, especially in the upper part of the core. From Table 5 it becomes clear that the main reason for this inconsistency lies in the accuracy of the transit time estimation, which is much underestimated in the case when the transit time is calculated from the neutron noise. For a complete understanding of the difference in transit time estimation, further investigations are planned to be performed.

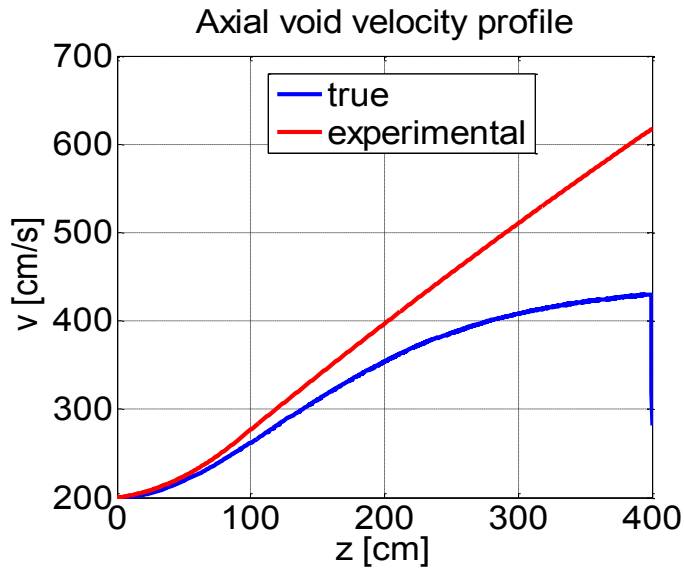


Fig. 13. Method 1. Axial void velocity profile as reconstructed from “experimental” transit times (estimated from the simulated neutron noise).

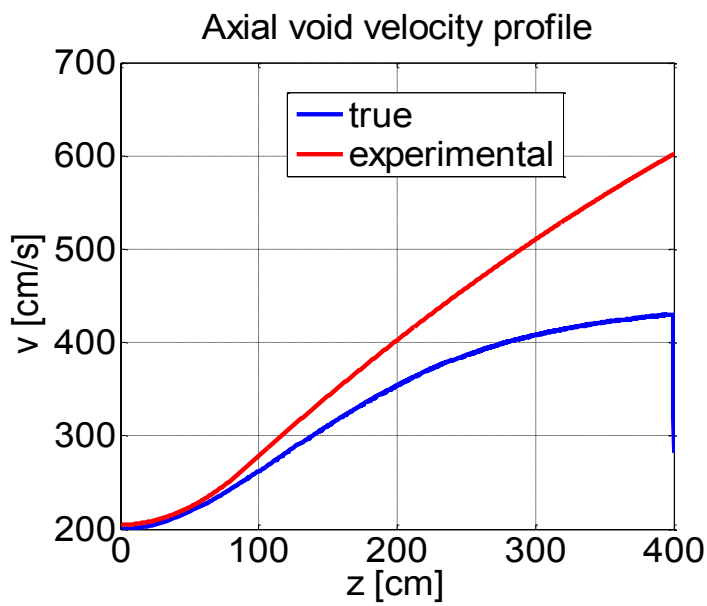


Fig. 14. Method 2. Axial void velocity profile as reconstructed from “experimental” transit times (estimated from the simulated neutron noise).

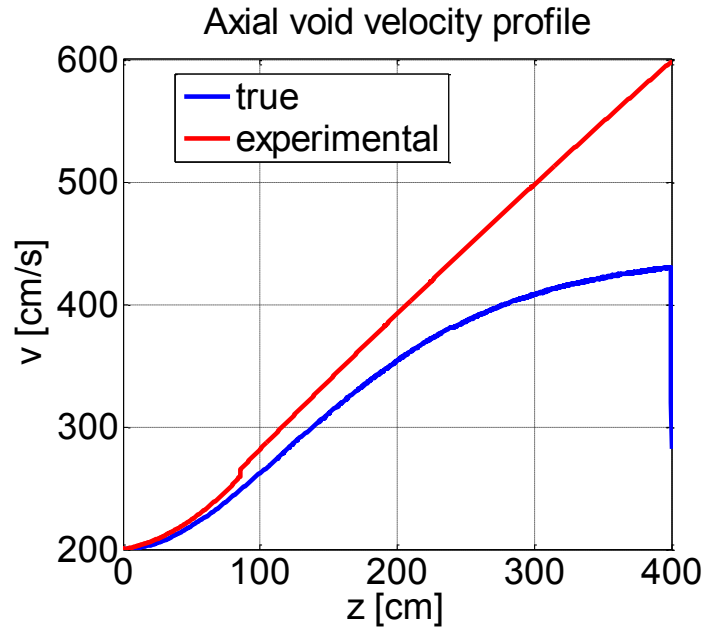


Fig. 15 Method 3. Axial void velocity profile as reconstructed from “experimental” transit times (estimated from the simulated neutron noise).

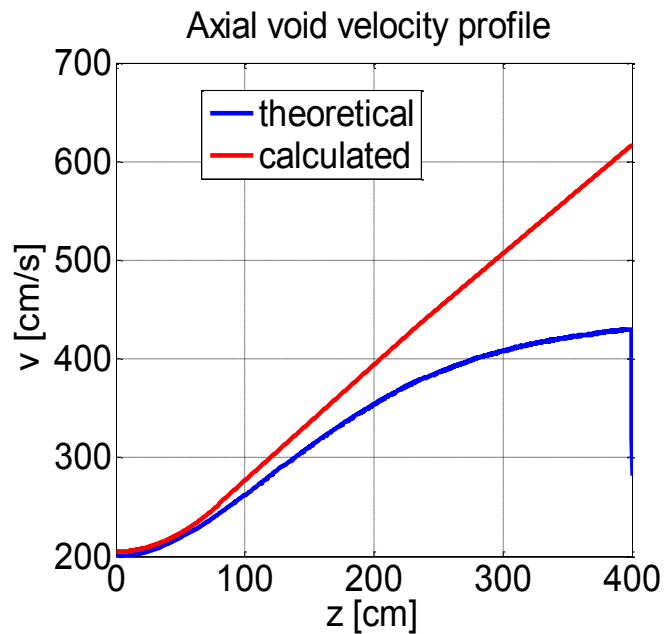


Fig. 16 Method 4. Axial void velocity profile as reconstructed from “experimental” transit times (estimated from the simulated neutron noise).

4.6. Conclusions

A simple two-dimensional model of the bubbly flow in a BWR heated channel is constructed to simulate the flow induced neutron noise detector signals. Thereafter, the corresponding neutron noise signals were calculated generated for six axial detector positions from this input.

Two different methods for estimating an axial void fraction were tested by processing the corresponding simulated neutron noise detector signals. The first method is based on the evaluation of the break frequency of the local component while the second one applies the transit time approach. From the comparison between the simulated and true results, one can conclude that the break frequency method shows a good qualitative agreement between the “true” and the reconstructed void profiles slightly overestimating the void fraction in the lower part of the core. The transit time method also shows quite promising results, except for the upper part of the channel where the transit time is underestimated. Thus, both methods are good candidates to apply for reconstructing the void profile from actual neutron noise measurements. However, additional measurements are required to successfully test both methods. For obvious reasons, the further work will mainly focus on the development and application of the second method and presented in the next Stage.

5. PROPOSAL FOR STAGE 15

The following items are proposed for Stage 15:

1. Application of the new curve fitting procedure, which was tested in the present Stage, to both new ex-core as well as in-core measurements, preferably three new measurements performed during one fuel cycle in R4.
2. Evaluation of new measurements made in R1, with the use of 4 LPRMs and one TIP detector, for testing the velocity and void fraction profile reconstruction methods, elaborated in the present Stage.
3. Investigation of the influence of the radial correlation length of the inlet temperature fluctuations on the noise level in PWRs.

A more concrete contract proposal will be sent to Ringhals regarding Stage 15.

6. ACKNOWLEDGEMENT

Stage 14 of the project was performed by funding from Ringhals Vattenfall AB, contract No. 614061-002. Contact person from Ringhals was Adj. Prof. Henrik Nylén.

7. REFERENCES

- [1] I. Pázsit, N. S. Garis, O. Thomson, and L. Norberg (1996), Analys av brusmätningar genomförda under perioden 93-94 vid Ringhals 3. CTH-RF-116/RR-2, Chalmers University of Technology, Gothenburg, Sweden

- [2] I. Pázsit (Editor) (1996), Final Report on the Research Project Ringhals Diagnostics and Monitoring, Stage 1. CTH-RF-122/RR-3, Chalmers University of Technology, Gothenburg, Sweden
- [3] I. Pázsit, J. Karlsson, and N. S. Garis (1997), Final Report on the Research Project Ringhals Diagnostics and Monitoring, Stage 2. CTH-RF-132/RR-4, Chalmers University of Technology, Gothenburg, Sweden
- [4] J. K.-H. Karlsson, and I. Pázsit (1998), Final Report on the Research Project Ringhals Diagnostics and Monitoring. Stage 3: Analysis of core barrel vibrations in Ringhals 2, 3 and 4 for several fuel cycles. CTH-RF-135/RR-5, Chalmers University of Technology, Gothenburg, Sweden
- [5] C. Demazière, V. Arzhanov, J. K.-H. Karlsson, and I. Pázsit (1999), Final Report on the Research Project Ringhals Diagnostics and Monitoring, Stage 4. CTH-RF-145/RR6, Chalmers University of Technology, Gothenburg, Sweden
- [6] C. Demazière, V. Arzhanov, and I. Pázsit (2000), Final Report on the Research Project Ringhals Diagnostics and Monitoring, Stage 5. CTH-RF-156/RR7, Chalmers University of Technology, Gothenburg, Sweden
- [7] C. Demazière, V. Arzhanov, and I. Pázsit (2001), Final Report on the Research Project Ringhals Diagnostics and Monitoring, Stage 6. CTH-RF-161/RR8, Chalmers University of Technology, Gothenburg, Sweden
- [8] C. Demazière, V. Arzhanov, and I. Pázsit (2002), Final Report on the Research Project Ringhals Diagnostics and Monitoring, Stage 7. CTH-RF-167/RR9, Chalmers University of Technology, Gothenburg, Sweden
- [9] C. Demazière, C. Sunde, V. Arzhanov, and I. Pázsit (2003), Final Report on the Research Project Ringhals Diagnostics and Monitoring, Stage 8. CTH-RF-177/RR10, Chalmers University of Technology, Sweden
- [10] C. Demazière, C. Sunde, and I. Pázsit (2005), Final Report on the Research Project Ringhals Diagnostics and Monitoring, Stage 9. CTH-RF-187/RR11, Chalmers University of Technology, Sweden
- [11] C. Sunde, J. Wright, C. Demazière and I. Pázsit (2005), Final Report on the Research Project Ringhals Diagnostics and Monitoring, Stage 10. CTH-RF-194/RR12, Chalmers University of Technology, Sweden
- [12] C. Sunde, C. Demazière and I. Pázsit (2007), Final Report on the Research Project Ringhals Diagnostics and Monitoring, Stage 11. CTH-NT-206/RR13, Chalmers University of Technology, Sweden
- [13] I. Pázsit, C. Demazière, C. Sunde, P. Bernitt and A. Hernández-Solís (2008), Final Report on the Research Project Ringhals Diagnostics and Monitoring, Stage 12. CTH-NT-220/RR-14, August 2008, Chalmers University of Technology, Sweden

- [14] I. Pázsit, C. Montalvo Martín, V. Dykin and T. Tambouratzis (2010) Final Report on the Research Project Ringhals Diagnostics and Monitoring, Stage 13. CTH-NT-230/RR-15, March 2010
- [15] R. Perez and D. N. Wood (1991) "Modeling and Analysis of Neutron Noise from an Ex-Core Detector at a PWR". Oak Ridge Nat. Lab.
- [16] F. J. Sweeney, J. March-Leuba and C. M. Smith, "Contributions of fuel vibrations to ex-core neutron noise during the first and second fuel cycles of the Sequoyah-1 pressurized water reactor". *Prog. Nucl. Energy* Vol. **15**, pp 283-290 (1985)
- [17] B. Severinsson, "Brusmätningar för analys av hårdhöljesvibrationer på Ringhals 4. Utförda mellan 2009-02-03 och 2009-04-23". Ringhals internal report, UH-rapport 2024043 / 3.0. April 2009.
- [18] M. Nilsson, "Brusmätning för att söka lågfrekventa störningar i R3, 100826. Ringhals internal report, UH-rapport 2099930 / 2.0. October 2010
- [19] R. Oguma, "A Method of Signal Transmission Path Analysis for Multivariate Random Processes". Report JAERI-M 84-084, [19]1984
- [20] D. Wach, G. Kosály (1974), Investigation of the joint effect of local and global driving sources in incore-neutron noise measurements. *Atomkernenergie*, vol.**23**, pp.224-250.
- [21] G. Kosály, L. Maróti, L. Meskó, (1975), A simple space dependent theory of the neutron noise in a boiling water reactor. *Annals of Nuclear Energy*, vol.2, pp.315-321.
- [22] I. Pázsit, Transport theory and stochastic processes, (2007), Lecture notes, Chalmers University of Technology, Sweden.
- [23] H.M. Hashemian, I. Jakubenko and V. Forej (1994), Measurements of core barrel-vibration and testing for core flow anomalies. Proceedings of the Specialist's Meeting on Instrumentation and Control of WWER Type Nuclear Power Plants, Prague, Czech Republic.
- [24] I. Pázsit, C. Demazière (2011), Noise Techniques in Nuclear Systems, Chapter in Handbook of Nuclear Engineering, Vol. 3, Reactors of Generation II, Springer, New York, USA.
- [25] I. Pázsit, O. Glöckler (1983), On the neutron noise diagnostics of PWR control rod vibrations I. Periodic vibrations, *Nucl. Sci. Engng*, Vol. 85, pp. 167-177.
- [26] I. Pázsit, O. Glöckler (1984), On the neutron noise diagnostics of PWR control rod vibrations II. Stochastic vibrations, *Nucl. Sci. Engng*, Vol. 88, pp. 77-87.
- [27] G. Kosály (1980), Noise investigations in boiling-water and pressurized-water reactors, *Prog. in Nuclear Energy*, Vol. 5, pp. 145-199.

-
- [28] I. Pázsit, O. Glöckler (1985), Cross sectional identification of two-phase flow by correlation technique, Prog. in Nuclear Energy, Vol. 15, pp. 661-669.
- [29] I. Pázsit (1986), Two-phase flow identification by correlation techniques, Ann. Nucl. Energy, Vol. 13, pp. 37-41.
- [30] F. B. Brown, T. M. Sutton (1996), Monte Carlo fundamentals, The 1996 Frederic Joliot summer school in reactor physics. Modern reactor physics and the modelling of complex systems proceedings, Cadarache & France, August 19-28, pp. 348-352.
- [31] D. Wach and G. Kosály (1974), Investigation of the joint effect of local and global driving sources in in-core neutron noise measurements, Atomkernenergie, Vol. 23, pp. 244-250.